

# Transmission Electron Microscopy and Neutron Powder Diffraction Studies of GdFeO<sub>3</sub> Type SrNbO<sub>3</sub>

H. Hannerz,\* G. Svensson,\* S. Ya. Istomin,† and O. G. D'yachenko†

\*Department of Structural Chemistry, Stockholm University, 10691 Stockholm, Sweden and †Chemical Department, Moscow State University, 119899 Moscow, Russia

Received December 7, 1998; in revised form April 23, 1999; accepted May 7, 1999

**Stoichiometric SrNbO<sub>3</sub>; with a GdFeO<sub>3</sub> type structure was synthesized between 1300 and 1550°C in Ar-filled and sealed niobium ampoules. Its crystal structure was refined using time-of-flight neutron diffraction data. Space group *Pnma*:  $a = \sqrt{2} \cdot a_p = 5.6894(2)$  Å;  $b = 2 \cdot a_p = 8.0684(1)$  Å;  $c = \sqrt{2} \cdot a_p = 5.6944(2)$  Å;  $R_{F2} = 0.020$ ; and  $R_p = 0.034$ . High-resolution electron microscopy and electron diffraction studies frequently revealed structural defects in SrNbO<sub>3</sub>. X-ray and electron diffraction studies showed cubic symmetry for SrNbO<sub>3</sub> synthesized below 1300°C and for compounds with nominal composition Sr<sub>0.8</sub>NbO<sub>3</sub> synthesized between 1200 and 1550°C. SrNbO<sub>3</sub> was found to be temperature independently paramagnetic.** © 1999 Academic Press

structures are found in the system CaNbO<sub>3</sub>–Ca(Ca<sub>1/3</sub>Nb<sub>2/3</sub>)NbO<sub>3</sub> (3).

In connection with our study of the perovskite-type solid solution Ca<sub>1-x</sub>Sr<sub>x</sub>NbO<sub>3</sub> (0 ≤ x ≤ 1.0), we performed a more detailed structural study of an orthorhombic modification of SrNbO<sub>3</sub> (10). During our work, an orthorhombic strontium-rich modification, Sr<sub>0.97</sub>NbO<sub>3</sub>, was reported by Peng *et al.* (11). A comparison between their results and ours will be given below. In the present work we thus report a synthesis, electron, and time-of-flight (TOF) neutron powder diffraction and high-resolution electron microscopy study of the orthorhombic modification of SrNbO<sub>3</sub>, as well as its magnetic properties.

## INTRODUCTION

A number of compounds with perovskite structure exhibit important physical properties such as superconductivity, giant magnetoresistance, or catalytic activity. Compounds with this structure are frequently found among complex niobium oxides with a  $d^0$ – $d^1$  electron configuration for Nb. NaNbO<sub>3</sub> (1) and KNbO<sub>3</sub> (2) are two examples of  $d^0$  compounds, and reduced oxoniobates with electron configurations between  $d^0$  and  $d^1$  are found with the alkaline-earth cations Ca (3), Sr (4–6), and Ba (5, 7, 8). Very often the perovskite structure is distorted, which strongly influences the properties of the compound. NaNbO<sub>3</sub>, for example, is found in seven modifications between –100 and 641°C at ambient pressure, one of which is ferroelectric and two antiferroelectric.

Among the reduced niobates ANb<sup>4+</sup>O<sub>3</sub> with A = Ca, Sr, or Ba, the ideal cubic perovskite structure is found for Sr<sub>x</sub>NbO<sub>3</sub> and Ba<sub>x</sub>NbO<sub>3</sub>. It has long been known that Sr<sub>x</sub>NbO<sub>3</sub> is nonstoichiometric with 0.70 ≤ x ≤ 0.95 (4). Ba<sub>x</sub>NbO<sub>3</sub> seems to be nearly stoichiometric with 0.95 ≤ x ≤ 1.0 (5, 7–9). Ca<sub>x</sub>NbO<sub>3</sub> (0.9 ≤ x ≤ 1.0) has an orthorhombic, distorted perovskite structure of the GdFeO<sub>3</sub> type (10). Calcium atoms can substitute for niobium in that compound, however, and a whole series of complicated super-

## EXPERIMENTAL

Powders of niobium (Aldrich 99.8%), Nb<sub>2</sub>O<sub>5</sub> (Roth 99.9%) and Sr<sub>5</sub>Nb<sub>4</sub>O<sub>15</sub> synthesized by heating SrCO<sub>3</sub> (Mallinckrodt 99.5%) and Nb<sub>2</sub>O<sub>5</sub> in air at 1000°C for 40 hours with an intervening regrinding were mixed according to the compositions Sr<sub>0.8</sub>NbO<sub>3</sub> and SrNbO<sub>3</sub>. The mixtures were pelletized and put in Nb ampoules which were then sealed by welding under Ar(g). The ampoules were annealed in argon in a high-temperature furnace at 1200, 1300, 1500, and 1550°C for 20–130 h. Monophasic or close to monophasic samples were obtained at 1500 and 1550°C after one thermal treatment. At 1200 and 1300°C, additional heating cycles with intervening regrinding were needed.

Thermogravimetric analyses (TGA) were performed with a SETARAM TAG 24 analyzer operated in air (100–1000°C, 5°C/min).

X-ray powder diffraction (XRD) photographs of all samples were recorded in a focusing camera of the Guinier–Hägg type, using CuK $\alpha_1$  radiation ( $\lambda = 1.54060$  Å) and Si as an internal standard.

Neutron TOF powder diffraction data were collected with the Polaris diffractometer at the U.K. spallation source ISIS at Rutherford Appleton Laboratory. Data from bank 2, covering  $d$ -values between 0.4 and 3.1 Å, were used for

structural refinement with the program package GSAS (12). Neutron scattering lengths of  $0.702 \cdot 10^{-12}$  cm for Sr,  $0.7054 \cdot 10^{-12}$  cm for Nb, and  $0.5805 \cdot 10^{-12}$  cm for O were used.

For the transmission electron microscopy (TEM) studies, small amounts of the sample were crushed in *n*-butanol. A drop of this dispersion was put on a holey carbon film supported by a copper grid. Electron diffraction (ED) and microanalysis (energy dispersive spectroscopy (EDS)) of the metal content were carried out with a JEOL JEM 2000 FX instrument operated at 200 kV. The microscope was equipped with a LINK QX200 energy dispersive detector in a high-angle position ( $70^\circ$ ).

Additional microanalyses of the same samples were performed with a JEOL JSM 880 scanning electron microscope (SEM). The cation content was calculated by averaging data from 20 crystallites.  $\text{Sr}_5\text{Nb}_4\text{O}_{15}$  was used as an external standard for the EDS analysis in both microscopes. A JEOL JEM 3010 instrument ( $1.7 \text{ \AA}$  point-to-resolution-point), operated at 300 kV, was used for the high-resolution electron microscopy (HREM) studies.

Magnetic measurements were carried out in a weak-field ac susceptometer (Lake Shore 7130) in the temperature range of 10–330 K, using a magnetic field of  $250 \text{ A m}^{-1}$  and a frequency of 500 Hz.

## RESULTS

All samples were red after the heat treatment: The sample with nominal composition  $\text{SrNbO}_3$  was ruby, and  $\text{Sr}_{0.8}\text{NbO}_3$  was dark red. The purity of the samples was strongly dependent on the synthesis temperature. Close to monophasic samples were obtained after 130 hours at  $1200^\circ\text{C}$ ; very few extraneous diffraction lines were seen. The

samples heated at  $1300^\circ\text{C}$  became almost single phase after 70 hours, yielding only very faint additional lines with maximum intensities  $< 1\%$ . Single-phase samples were obtained at 1500 and  $1550^\circ\text{C}$ .

SEM-EDS analysis of the metal ratio in monophasic  $\text{SrNbO}_3$  synthesized at  $1550^\circ\text{C}$  resulted in  $\text{Sr}_{1.06(2)}\text{NbO}_3$ , whereas the TEM-EDS analysis yielded  $\text{Sr}_{0.99(5)}\text{NbO}_3$ . A TGA study of the same sample resulted in a weight increase of 3.52%, corresponding to the composition  $\text{Sr}_{1.00}\text{NbO}_3$ .

The X-ray powder diffraction pattern of  $\text{SrNbO}_3$  revealed a clear splitting of some reflections but no extra lines. The XRD pattern of  $\text{SrNbO}_3$  and an enlargement of the split  $200_{\text{per}}$  and  $310_{\text{per}}$  reflections are shown in Fig. 1. The XRD patterns could be indexed with tetragonal unit cells where  $a \approx c \approx a_{\text{per}}$ ; see Table 1. The XRD patterns of  $\text{Sr}_{0.8}\text{NbO}_3$  indicated cubic symmetry as there were no visible splittings of the reflections

The SEM-EDS and the TGA measurements of the  $\text{Sr}_{0.8}\text{NbO}_3$  sample resulted in the compositions  $\text{Sr}_{0.94(2)}\text{NbO}_3$  and  $\text{Sr}_{0.92}\text{NbO}_3$ , respectively. The slightly high strontium content, compared with the nominal, is in agreement with the unit-cell parameters from XRD data. Ridgley *et al.* (4) showed that there is a Vegard's law relationship between unit-cell dimension and strontium content for the cubic perovskite  $\text{Sr}_x\text{NbO}_3$ . Thus,  $a_{\text{per}} = 4.012(1) \text{ \AA}$  obtained for  $\text{Sr}_{0.8}\text{NbO}_3$  corresponds to  $\text{Sr}_{\sim 0.9}\text{NbO}_3$ , in agreement with the results above. The excess strontium content above nominal may be explained by the presence of small amounts of unreacted niobium metal or niobium suboxides not seen in the XRD patterns.

The magnetic measurements showed that  $\text{SrNbO}_3$  has a temperature-independent paramagnetic susceptibility, see Fig. 2. We reported earlier that  $\text{SrNbO}_3$  is a metal-like

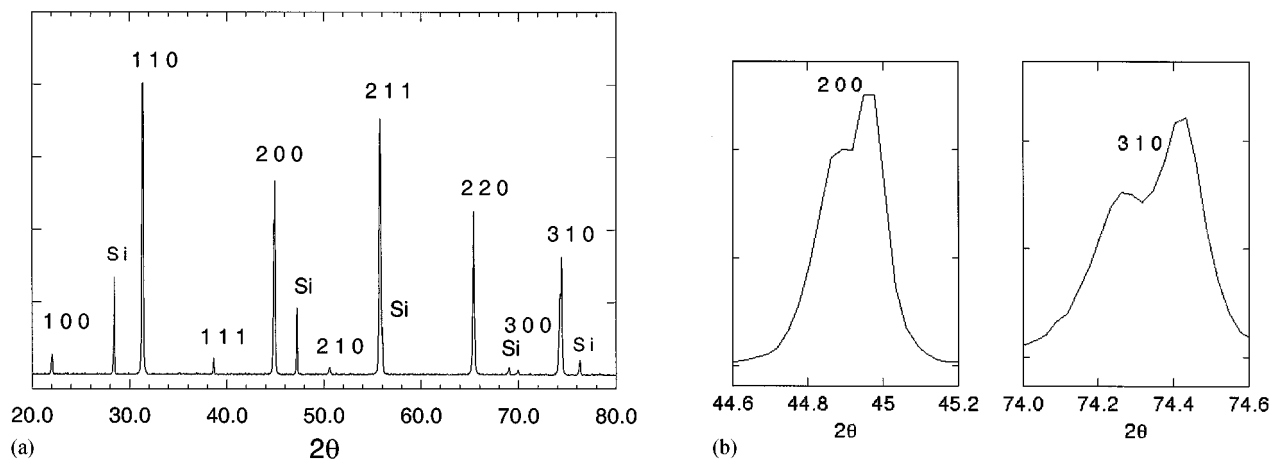


FIG. 1. (a) X-ray powder diffraction pattern of  $\text{SrNbO}_3$  synthesized at  $1550^\circ\text{C}$ . (b) Detail of the diffraction pattern in (a) showing the split  $200_{\text{per}}$  and  $310_{\text{per}}$  reflections.

**TABLE 1**  
Unit-Cell Parameters of Cubic Sr<sub>0.8</sub>NbO<sub>3</sub> Samples and the Tetragonal Subcells of the SrNbO<sub>3</sub> Sample

Composition	x = 0.8		x = 1.0	
Temperature	a/Å	a/Å	c/Å	
1300°C	3.9967(2)	4.0237(4)	4.0310(5)	
1500°C	3.9999(2)	4.025(1)	4.031(1)	
1550°C	4.012(1)	4.025 (1)	4.032(1)	

conductor (10). Our results corroborate those published by Peng *et al.* (11)

### Electron Diffraction Studies

The  $x = 0.8$  and 1.0 samples synthesized at 1300 and 1550°C were investigated by electron diffraction. The TEM-ED patterns of the crystallites in the Sr<sub>0.8</sub>NbO<sub>3</sub> sample contained no superstructural reflections, whereas a superstructure was found in all SrNbO<sub>3</sub> crystallites. ED patterns of SrNbO<sub>3</sub> along  $\langle 100 \rangle_{\text{per}}$  and  $\langle 110 \rangle_{\text{per}}$  with superstructural reflections corresponding to a  $\sqrt{2} \cdot a_{\text{per}}$  supercell are shown in Fig. 3. The tetragonal distortion of the perovskite subcell parameters  $a_{\text{per}}$  and  $c_{\text{per}}$  obtained from the XRD patterns of SrNbO<sub>3</sub> is too small to be revealed by the selected-area ED patterns. Streaking and superstructural reflections along the perovskite subaxis are present in other ED patterns, suggesting a doubling of all perovskite axes. Figure 4, for example, is an  $hk0_{\text{per}}$  pattern, which has been tilted to show both the zero and first-order Laue zones. Among  $hk0_{\text{per}}$  and  $hk1_{\text{per}}$  there are reflections consistent with an  $a = b \approx 2 \cdot a_{\text{per}}$  super cell. The arrowed row of reflections halfway between the  $hk0$  and  $hk1$  layers is also consistent with a doubling ( $c \approx 2 \cdot a_{\text{per}}$ ) in that direction, suggesting  $a = b = c = 2 \cdot a_{\text{per}}$ . However, the ED pattern

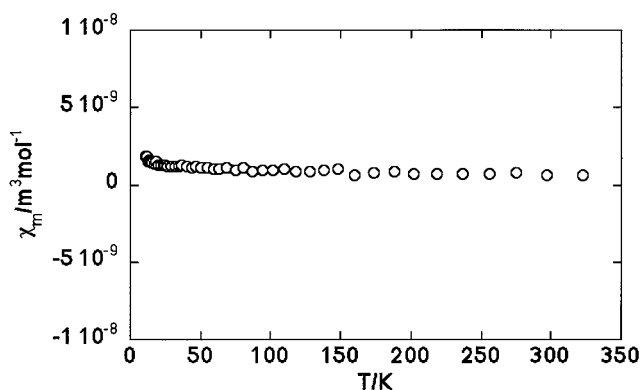


**FIG. 2.** Magnetic susceptibility ( $\text{m}^3 \text{mol}^{-1}$ ) versus temperature for orthorhombic SrNbO<sub>3</sub>.

corroborates an  $a \approx \sqrt{2} \cdot a_{\text{per}}$  and  $c \approx 2 \cdot a_{\text{per}}$  supercell as well, if the crystal is severely twinned.

### Neutron Powder Diffraction Studies

Several superstructural reflections were observed in the TOF neutron diffraction pattern shown in Fig. 5, indicating a larger unit cell in agreement with the ED studies. It can be indexed with a tetragonal unit cell where  $a \approx \sqrt{2} \cdot a_{\text{per}}$  and  $c \approx 2 \cdot a_{\text{per}}$  with the reflection condition  $00l: l = 2n$  and with the alternative cell  $a \approx 2 \cdot a_{\text{per}}$  and  $c \approx 2 \cdot a_{\text{per}}$  with the reflection conditions  $hk0: h + k = 2n$  and  $0kl: k + l = 2n$ . The possibility of an orthorhombic unit cell must also be considered.

The observed reflection conditions for the tetragonal  $a = \sqrt{2} \cdot a_{\text{per}}$ ,  $c = 2 \cdot a_{\text{per}}$  unit cell ( $00l: l = 2n$ ) suggested the space groups  $P4_2$  (77),  $P4_2/m$  (84), or  $P4_222$  (93), and for the  $a = 2 \cdot a_{\text{per}}$ ,  $c = 2 \cdot a_{\text{per}}$  unit cell ( $hk0: h + k = 2n$ ,  $0kl: k + l = 2n$ ) the space group  $P4_2/nmm$  (134). Each of these symmetries was tested, but the refinements did not converge properly. We therefore tried some other tetragonal space groups with slightly different extinction conditions both for the  $a = \sqrt{2} \cdot a_{\text{per}}$  and  $c = 2 \cdot a_{\text{per}}$  cell (space groups:  $P4_2/mmc$  and (131),  $P4_2/mcm$  (132)) and the  $a = 2 \cdot a_{\text{per}}$  and  $c = 2 \cdot a_{\text{per}}$  cell (space groups:  $P4_2/n$  (86),  $P4_2nm$  (102),  $P4nc$  (104),  $P4n2$  (118),  $P4/nbm$  (125),  $P4/nnc$  (126),  $P4/mnc$  (128),  $P4/ncc$  (130),  $P4_2/nbc$  (133),  $P4_2/nmm$  (134),  $P4_2/nmc$  (137), and  $P4_2/ncm$  (138)). The best result was obtained in  $P4_2/nmc$ :  $R_{\text{wp}} = 0.043$ ,  $R_{\text{F}^2} = 0.032$ ,  $\chi^2 = 4.0$ , using the  $a \approx 2 \cdot a_{\text{per}}$  and  $c \approx 2 \cdot a_{\text{per}}$  supercell, but the refinement was not stable. (This refinement included fractional coordinates and individual isotropic temperature factors.) Damping was needed for all parameters to reach convergence, which together with the high  $\chi^2$  value indicated also that this space group was wrong.

We therefore decided to try some orthorhombic space groups and found it possible to refine the structure in the closely related space groups  $Pnma$  (62) with the unit-cell parameters  $a \approx c \approx \sqrt{2} \cdot a_{\text{per}}$ ,  $b \approx 2 \cdot a_{\text{per}}$ , and  $Cmcm$  (63) with parameters  $a \approx b \approx c \approx 2 \cdot a_{\text{per}}$ . Refinement of the structure in  $Pnma$  and  $Cmcm$ , using isotropic temperature factors, resulted in  $R_{\text{wp}} = 0.028$ ,  $R_{\text{p}} = 0.038$ ,  $R_{\text{F}^2} = 0.040$ ,  $\chi^2 = 2.29$  and  $R_{\text{wp}} = 0.027$ ,  $R_{\text{p}} = 0.038$ ,  $R_{\text{F}^2} = 0.039$ ,  $\chi^2 = 2.25$ , respectively. No damping was needed during the final refinement cycles. The main difference between the space groups is the presence of the 112 and 332 reflections in the  $a \approx b \approx c \approx 2 \cdot a_{\text{per}}$   $Cmcm$  model. These reflections are not seen in neutron diffraction patterns, and their calculated intensity is  $< 1\%$ . The small difference in  $R$ -values between the  $Pnma$  and  $Cmcm$  models led us to choose the  $Pnma$  alternative as it implies a smaller unit cell.

The  $R$ -values for different refinements of the model are given in Table 2. Introducing anisotropic temperature

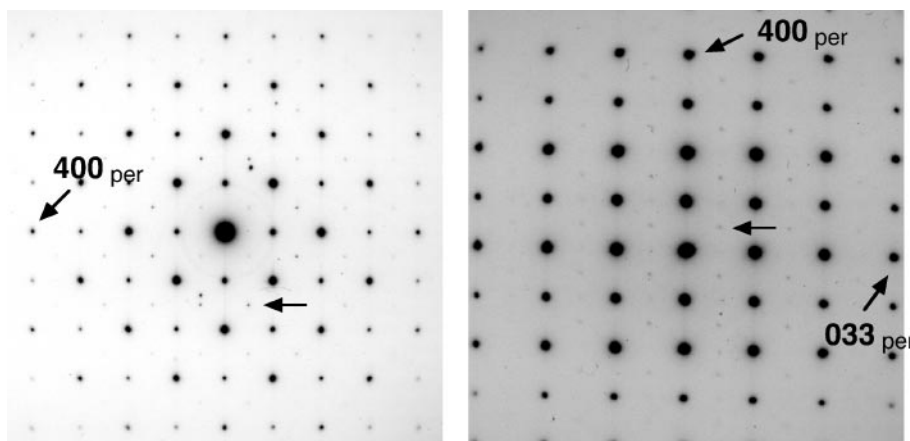


**FIG. 3.** Electron diffraction patterns of orthorhombic SrNbO<sub>3</sub> along (left)  $\langle 100 \rangle_{\text{per}}$  and (right)  $\langle 110 \rangle_{\text{per}}$ . A superstructural reflection in each pattern is marked.

factors for all atoms resulted in a considerable lowering of the  $R$ -factors:  $R_{\text{wp}} = 0.020$ ,  $R_{\text{p}} = 0.034$ ,  $R_{\text{F}^2} = 0.020$ , and  $\chi^2 = 1.27$ . The corresponding observed, calculated, and difference neutron diffraction patterns are shown in Fig. 5. Refined parameters were scale factor, eight background parameters (shifted Chebyshev), twenty anisotropic temperature factors, three unit-cell parameters, seven fractional coordinates, three profile coefficients (pseudo-Voigt), extinction, absorption, and zero shift. The atomic fractional parameters and the anisotropic temperature factors ( $U_{\text{anis}}$ ) are given in Tables 3 and 4, respectively.

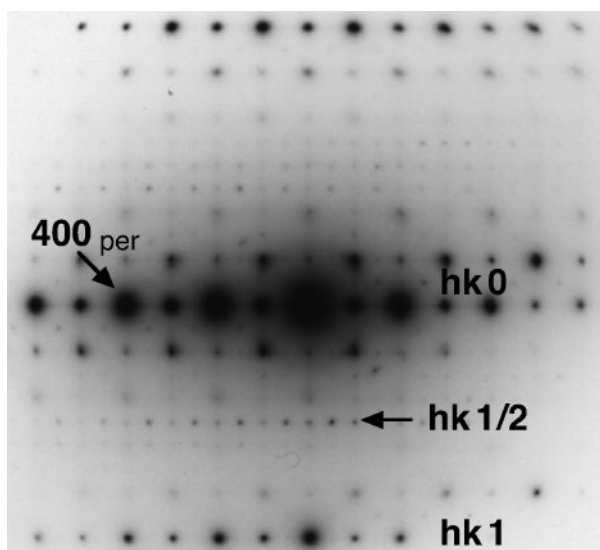


**FIG. 4.** Electron diffraction pattern of a tilted crystallite to show ZOLZ ( $hk0$ ) and FOLZ ( $hk1$ ). There are superstructural reflections in the  $hk0$  and  $hk1$  layers corresponding to  $2 \cdot a_{\text{p}}$  and  $2 \cdot a_{\text{p}}$ . The line of spots at  $hk1/2$  indicates a  $2 \cdot a_{\text{p}}$  unit cell in that direction as well.

Refinement of the strontium occupancy (fixed isotropic temperature factors for Sr) resulted in  $x = 0.986(3)$ , although the model did not improve very much, see Table 2. (This value is in excellent agreement with the EDS and the TGA results where  $x = 0.99(5)$  and  $x = 1.00$ , respectively.) Refinements of the niobium and oxygen occupancies resulted in nonphysical values.

The structural model obtained for SrNbO<sub>3</sub> is a GdFeO<sub>3</sub>-type distorted perovskite structure, like that reported for CaNbO<sub>3</sub> (10). During the writing of this article a structural determination of Sr<sub>0.97</sub>NbO<sub>3</sub> by Peng *et al.* appeared (11). They used high-resolution powder neutron diffraction data to refine the structure in space group  $P2_12_12$ . They report rather high  $R$ -values, and their resulting model differs significantly from ours. We tried to refine the structure using their model with our data, but the refinement did not converge.

It is possible to distinguish between the space groups  $Pnma$  and  $P2_12_12$  using convergent beam electron diffraction patterns recorded along the  $2 \cdot a_{\text{per}}$  axis being  $[010]$  in  $Pnma$  and  $[001]$  in  $P2_12_12$  (13). The space group  $Pnma$  will give electron diffraction patterns where the symmetry for both bright field (BF) and whole pattern (WP) (higher Laue zones are included) are  $2mm$ . For  $P2_12_12$  the same symmetry will be found for the BF pattern while it would be 2 for the WP pattern. A BF and a WP pattern of SrNbO<sub>3</sub> along  $[010]_{Pnma}$  are shown in Figs. 6a and 6b, respectively. The symmetry of both patterns is  $2mm$  in agreement with space group  $Pnma$ .

The reason for the discrepancy between our result and that reported by Peng *et al.* (11) is unclear. They have in fact used a slightly different synthetic route by annealing their samples in flowing Ar(g) at 1400°C, although we do not believe this is the reason. However, it should be noted that they have not tested the space groups  $Pnma$  or  $Cmcm$ .

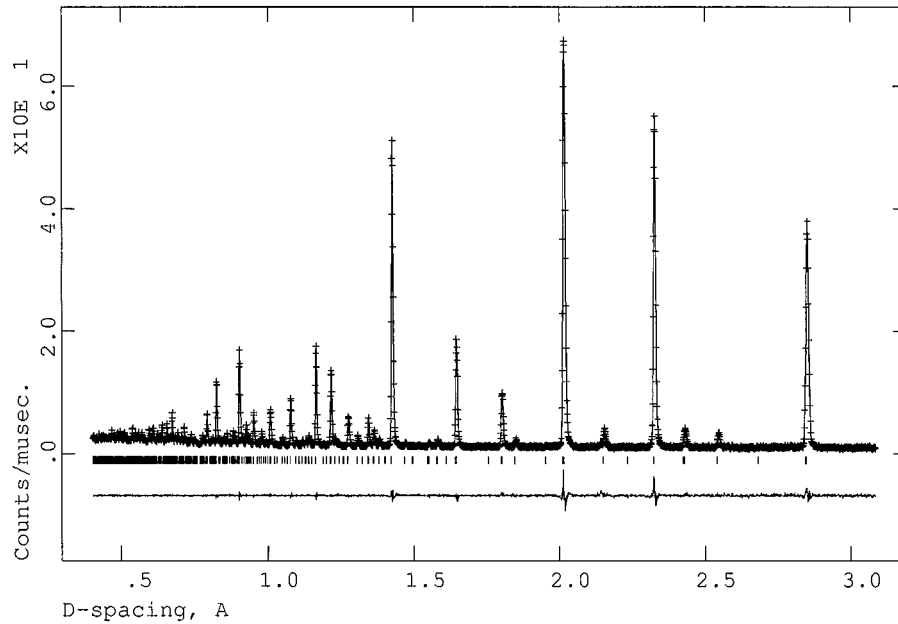


FIG. 5. Observed, calculated, and difference intensities time-of-flight neutron diffraction pattern.

### HREM Studies

HREM images such as Fig. 7 showed that most of the crystallites were twinned and contained extended defects, in

contrast to reports on  $K_xBa_{1-x}NbO_3$  (14). A closer inspection of the HREM image in Fig. 7 reveals domains with  $\sqrt{2} \cdot a_{\text{per}} \times \sqrt{2} \cdot a_{\text{per}}$  lattice fringes, as well as such with  $\sqrt{2} \cdot a_{\text{per}} \times 2 \cdot a_{\text{per}}$  fringes. No crystallites or domains with

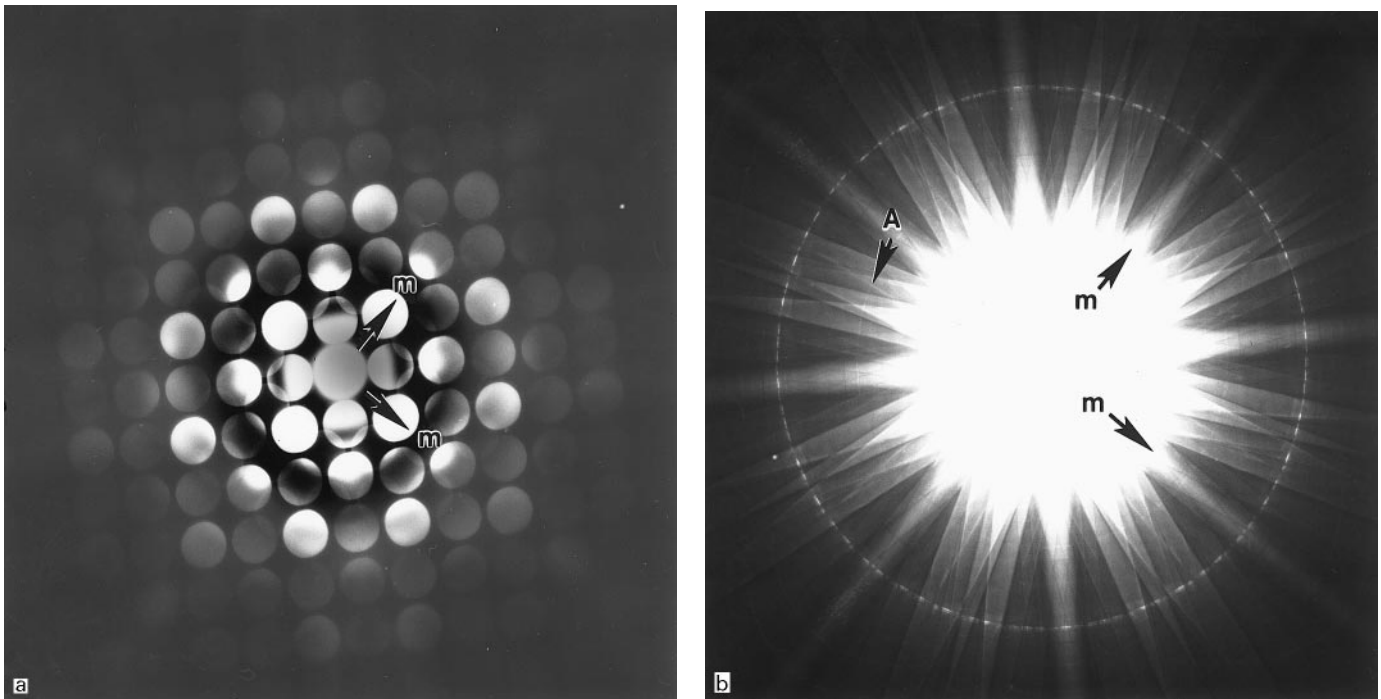


FIG. 6. (a) Bright field electron diffraction pattern taken along  $[010]_{Pnma}$  revealing the symmetry  $2mm$ . (b) The symmetry of the whole pattern (WP), including ZOLZ and HOLZ, is  $2mm$  in agreement with that expected for space group  $Pnma$ .  $P2_12_12$  would give a WP with the symmetry  $m$ .

**TABLE 2**  
**R-Values for Different Refinement Models of SrNbO<sub>3</sub>**

	$R_{wp}^a$	$R_p^b$	$R_{F^2}^c$	$\chi^2{}^d$
$U_{iso}(Sr,Nb,O)$	0.0275	0.0378	0.040	2.288
$U_{iso}(Sr,Nb,O), Sr_{occ}$	0.0274	0.0377	0.040	2.276
$U_{iso}(Sr,Nb), U_{anis}(O)$	0.0233	0.0357	0.023	1.642
$U_{iso}(Nb), U_{anis}(Sr, O)$	0.0206	0.0349	0.0205	1.284
$U_{anis}(Sr,Nb,O)$	0.0204	0.0343	0.0203	1.269
$U_{anis}(Sr,Nb,O), Sr_{occ}$	0.0203	0.0344	0.0198	1.248

$$^a R_{wp} = \sqrt{\sum w(I_o - I_c)^2 / \sum w \cdot I_o^2}$$

$$^b R_p = \sum |I_o - I_c| / \sum I_o^2$$

$$^c R_{F^2} = \sum |F_o^2 - F_c^2| / \sum F_o^2$$

$$^d \chi^2 = \sum w(I_o - I_c)^2 / (N_{obs} - N_{var})$$

$2 \cdot a_{per} \times 2 \cdot a_{per}$  fringes were observed, however, in agreement with the space group  $Pnma$ .

The structural defects found in the HREM images frequently run zigzag through the crystal, alternatingly parallel to  $\{100\}_{per}$  and  $\{010\}_{per}$ , which involves a  $1/2 \cdot \{110\}_{per}$  shift parallel to the defect. However, occasionally the defects run diagonally in the perovskite structure. An HREM image of higher magnification of a crystal with a defect is shown in

**TABLE 3**

**Atomic Positions and Displacement Parameters for SrNbO<sub>3</sub>**

Space group $Pnma$ , $Z = 4$ , $a = 5.6894(2) \text{ \AA}$ , $b = 8.0684(1) \text{ \AA}$ , $c = 5.6944(2) \text{ \AA}$					
Position	Atom	$x$	$y$	$z$	$U_i/U_{eq}^a \times 100$
4b	Nb(1)	0	0	0.5	0.26 <sup>a</sup>
4c	Sr(1)	0.0059(3)	1/4	0.001(1)	0.98 <sup>a</sup>
4c	O(1)	0.4973(6)	1/4	0.0246(4)	0.94 <sup>a</sup>
8d	O(2)	0.2695(3)	0.0135(2)	0.7282(3)	0.86 <sup>a</sup>

<sup>a</sup> Anisotropically refined; see Table 4.

Fig. 8a. This defect does not start at the edge of the crystallite. A possible interpretation is that the HREM image reveals how a SrO layer involving a structural shift along  $1/2 \cdot \{110\}$  can be incorporated in the structure, as shown in Fig. 8b. This results in a  $K_2NiF_4$  structural element like that found in  $Rb_2LaNb_2O_7$  (15). Image simulations indicate that the thickness of the crystal varies from 20 Å at A to 60 Å at C in the image. It should be noted that the number of defects observed is too low to affect the composition of SrNbO<sub>3</sub>.

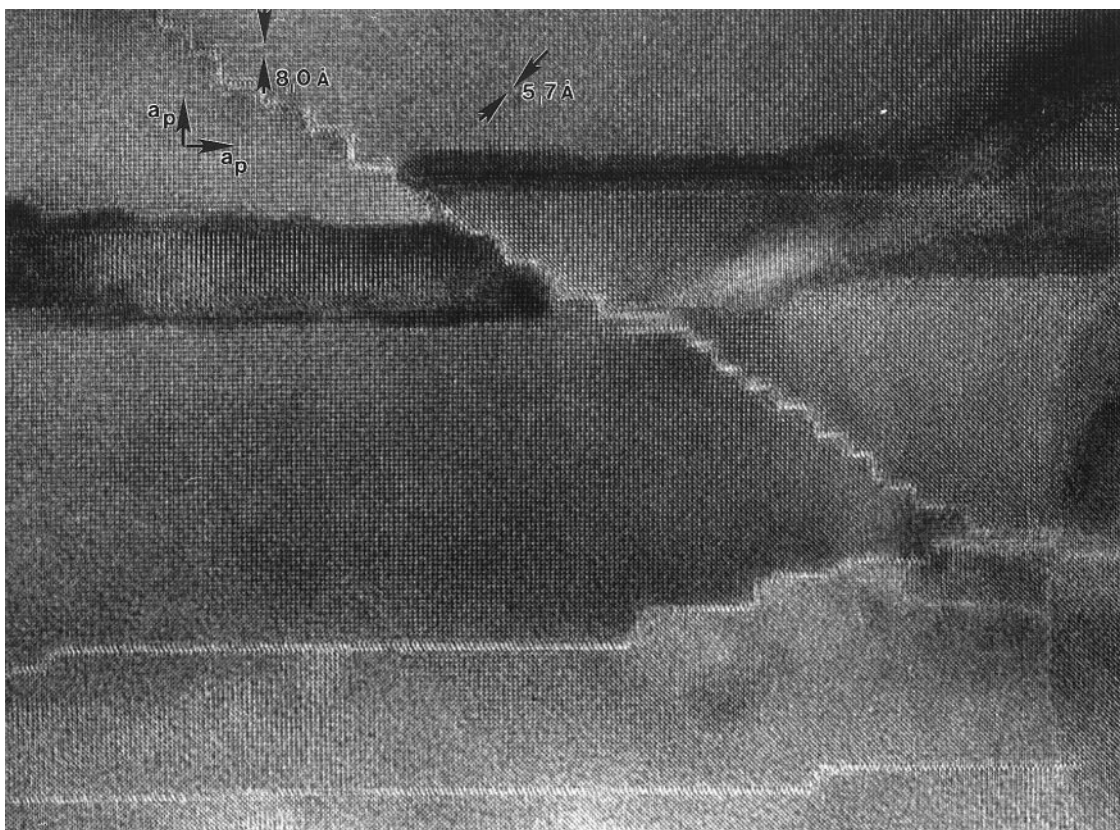


**FIG. 7.** HREM images of SrNbO<sub>3</sub> along  $\{100\}_{per}$  showing defects along  $\{100\}_{per}$  and  $\{010\}_{per}$ . The lattice fringes corresponding to  $a = 2 \cdot a_{per}$  and  $a = \sqrt{2} \cdot a_{per}$  are marked.

**TABLE 4**  
Anisotropic Displacement Parameters<sup>a</sup> multiplied by 100.0

Atom	$U_{11}$	$U_{22}$	$U_{33}$	$U_{12}$	$U_{13}$	$U_{23}$
Nb1	0.06(4)	0.43(3)	0.29(5)	-0.08(4)	-0.03(9)	0.01(6)
Sr1	0.31(4)	0.85(4)	1.79(7)	0.00	-0.26(3)	0.00
O1	1.36(7)	0.42(4)	1.04(7)	0.00	0.0(1)	0.00
O2	0.56(5)	1.14(4)	0.87(6)	-0.14(4)	-0.50(2)	0.13(5)

$$^a U_{\text{anis}} = e^{-2 \cdot \pi^2 (a^{*2} \cdot h^2 \cdot u_{11} + \dots + 2 \cdot h \cdot k \cdot u_{12} \cdot a^* \cdot b^*)}$$

## DISCUSSION

The interatomic distances in SrNbO<sub>3</sub> are given in Table 5, and Fig. 9 shows a structural model using the coordinates in Table 3. SrNbO<sub>3</sub> has a distorted perovskite structure of the GdFeO<sub>3</sub> type, similar to that found in LnTiO<sub>3</sub>; Ln = La, Nd, Sm, Gd, (16); SrZrO<sub>3</sub> (17); and CaNbO<sub>3</sub> (10). The shift of the metal atom positions from those found in cubic perovskite is very small. The niobium atoms are at the ideal positions in cubic perovskite, and the strontium atoms are only displaced by 0.033 Å from the ideal position. This latter shift is smaller than those found in SrZrO<sub>3</sub> (0.15 Å) and CaNbO<sub>3</sub> (0.27 Å). The cuboctahedron of oxygen atoms around the Sr atom is distorted with Sr–O interatomic distances between 2.676(3) and 3.057(3) Å. The distortion is smaller than in CaNbO<sub>3</sub> (10) and SrZrO<sub>3</sub> (16). This is not surprising, considering the smaller size of the calcium ion and the  $d^0$  electron configuration of the zirconium(IV) atom (18). The NbO<sub>6</sub> octahedron in Sr<sub>0.98</sub>NbO<sub>3</sub> is rather regular with  $d_{\text{Nb-O}1} = 2.0221(2)$  Å,  $d_{\text{Nb-O}2'} = 2.013(2)$  Å, and  $d_{\text{Nb-O}2''} = 2.032(2)$  Å. The tilts of the NbO<sub>6</sub> octahedra are  $a^-c^+a^-$ , using the notation described by Glazer (19). The angles between the NbO<sub>6</sub> octahedra are Nb–O1–Nb = 172.0(1)° and Nb–O2–Nb = 168.7(1)°, which is larger than found in CaNbO<sub>3</sub> (153° and 151°) and SrZrO<sub>3</sub> (156.2° and 157.8°).

In contrast to the work presented here, the structure of Sr<sub>0.97</sub>NbO<sub>3</sub> reported by Peng *et al.* (11) contains significantly distorted NbO<sub>6</sub> octahedra:  $d_{\text{Nb-O}} = 1.957$  to 2.062 Å. These authors also report a smaller tilt of the NbO<sub>6</sub> octahedra: Nb–O–Nb 174.2° and 179.9°.

**TABLE 5**  
Selected Interatomic Distances (Å) and Angles with E.S.D. in Parentheses

Nb–O(1)	2 ×	2.0220(2)	Sr(1)–O(1)	2.994(6)
Nb–O(2)	2 ×	2.013(2)	Sr(1)–O(1)	2.897(4)
Nb–O(2)	2 ×	2.032(2)	Sr(1)–O(1)	2.799(3)
			Sr(1)–O(2)	2.701(6)
Angle	Degrees		Sr(1)–O(2)	2 × 2.882(4)
Nb–O(1)–Nb		172.0(1)	Sr(1)–O(2)	2 × 2.798(3)
Nb–O(2)–Nb		168.7(1)	Sr(1)–O(2)	2 × 3.058(3)
			Sr(1)–O(2)	2 × 2.676(3)

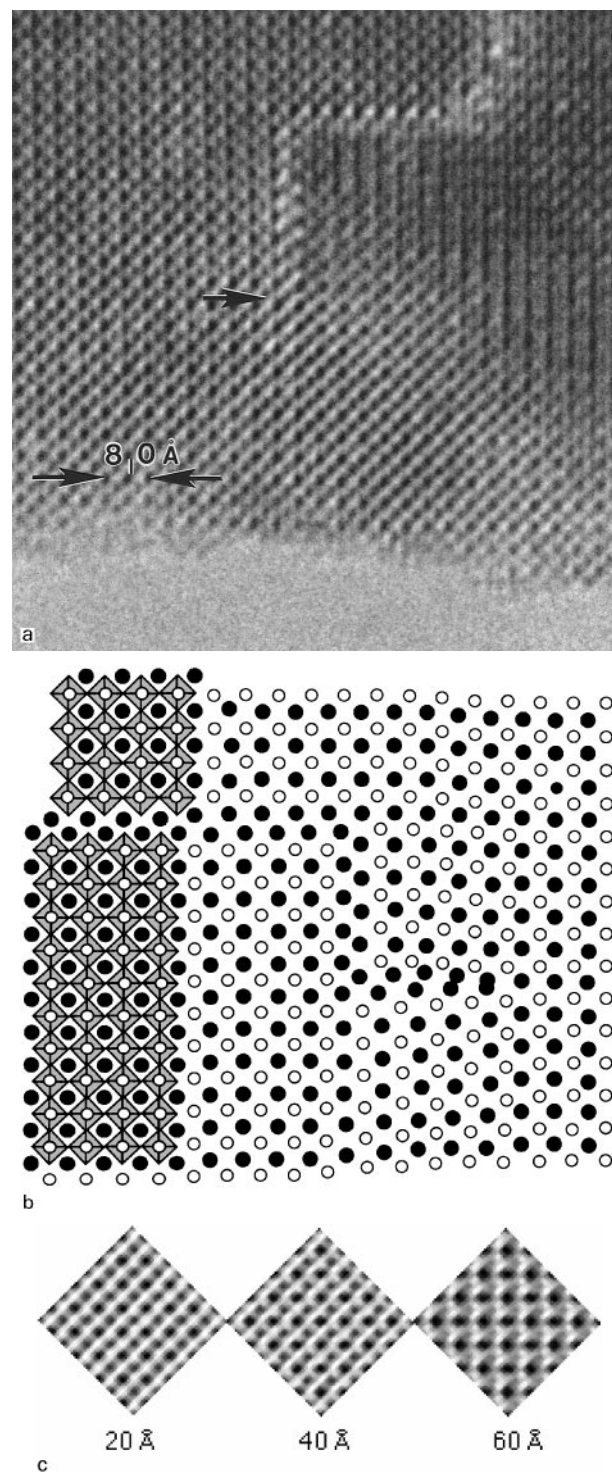


**FIG. 8.** (a) HREM image of a  $\{100\}_{\text{per}}$  defect running zigzag through the crystal. The thicknesses of the crystallite are  $\sim 20$  Å at A and  $\sim 60$  Å at B according to the image simulations in (c). (b) A tentative interpretation of the defect in (a) showing how a SrO layer involving a structural shift along  $1/2 \cdot \{110\}$  can be incorporated in the SrNbO<sub>3</sub> structure. (c) Image simulations of SrNbO<sub>3</sub> using the atomic coordinates in Table 3. (Defocus =  $-350$  Å (Scherzer focus =  $-412$  Å); thickness = 20, 40, and 60 Å, objective aperture = 0.5 Å, beam tilt = 0.5 mrad along  $[101]_{Pnma}$ . The simulations were performed with the MacTempas program.)

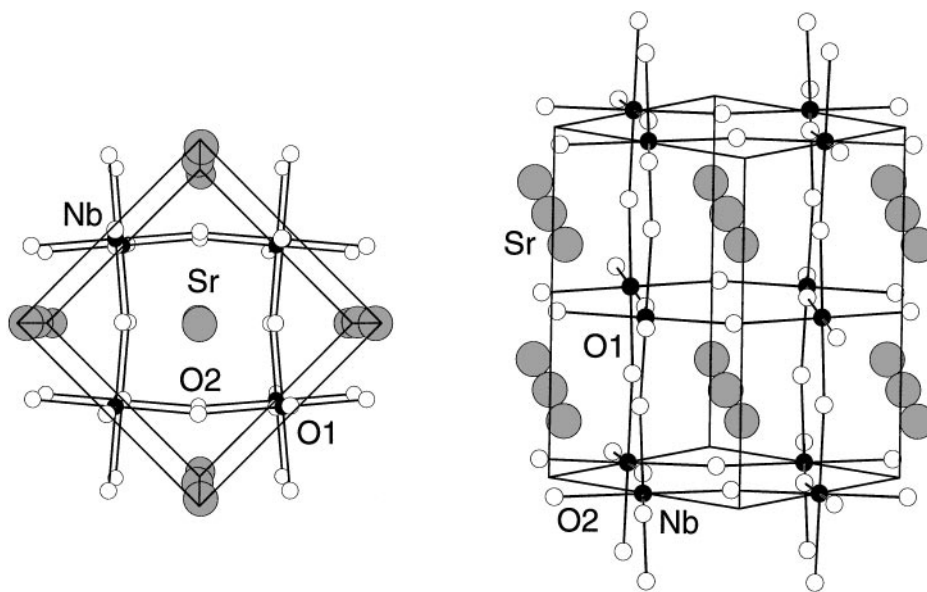


FIG. 9. The crystal structure of orthorhombic  $\text{SrNbO}_3$ .

At present there is no obvious explanation for the  $\text{GdFeO}_3$  type distortion found in  $\text{SrNbO}_3$  synthesized at high temperatures. According to Goldsmith (20),  $\text{SrNbO}_3$  with a  $t$ -value ( $t = (r_A + r_O)/\sqrt{2}(r_B + r_O)$ ) of 0.95 should adopt the ideal cubic perovskite structure. One reason for the apparent anomaly could be formation of oxygen vacancies, but their number has to be very small since both the TGA measurements and the structural refinement indicate that all oxygen positions are fully occupied.

An alternative and more probable explanation is that the maximum Sr content approaches 1.0 when synthesized at high temperatures. The high strontium content then induces a tilt of the  $\text{NbO}_6$  octahedra. There should be a continuous increase in distortion when going from  $\text{BaNbO}_3$  over  $\text{SrNbO}_3$  to  $\text{CaNbO}_3$ .

#### ACKNOWLEDGMENTS

The authors thank Dr. Pedro Berastegui at ISIS, Rutherford, for collecting the data and Prof Mats Nygren for valuable discussions and TGA measurements. This work was supported by the Swedish Natural Science Research Council (NFR), the Royal Swedish Academy of Sciences, and the Russian Fundamental Research Foundation (Grant No. 97-03-33432a).

#### REFERENCES

1. M. Ahtee, A. M. Glazer, and H. D. Megaw, *Philos. Mag.* **26**, 995, (1972)
2. L. Katz, H. D. Megaw, *Acta Crystallogr.* **22**, 639 (1967).

3. M. Hervieu, F. Studer, and B. Raveau, *J. Solid State Chem.* **22**, 273 (1977).
4. D. Ridgley and R. J. Ward, *J. Am. Chem. Soc.* **77**, 6132 (1955).
5. B. Hessen, S. A. Sunshine, T. Siegrist, and R. Jimenez, *Mater. Res. Bull.* **26**, 85 (1991).
6. K. Isawa, J. Sugiyama, K. Matsuura, A. Nozaki, and H. Yamauchi, *Phys. Rev. B* **47**, 2849 (1993).
7. R. R. Kreiser, and R. Ward, *J. Solid State Chem.* **1**, 368 (1970).
8. G. Svensson, and P.-E. Werner, *Mater. Res. Bull.* **25**, 9 (1990).
9. M. T. Casais, J. A. Alonso, I. Rasines, and M. A. Hidalgo, *Mater. Res. Bull.* **30**, 201 (1995).
10. S. Ya. Istomin, G. Svensson, O. G. D'yachenko, W. Holm, and E. V. Antipov, *J. Solid State Chem.* **141**, 514 (1998).
11. N. Peng, J. T. S. Irvine, and A. G. Fitzgerald, *J. Mater. Chem.* **8**, 1033 (1998).
12. A. C. Larson and R. B. von Dreele, The General Structure Analysis System, MS-H805, Los Alamos National Laboratory, 1991.
13. B. F. Buxton, J. A. Eades, J. W. Steeds, and G. M. Rackham, *Proc. R. Soc. (London) A* **281**, 171 (1976)
14. C. Chaillout, E. Gautier, E. M. Kopnin, E. V. Antipov, and M. Marezio, *J. Solid State Chem.* **123**, 236 (1996).
15. A. R. Armstrong and P. A. Anderson, *Inorg. Chem.* **33**, 4366 (1994).
16. D. A. MacLean, H.-N. Ng, and J. E. Greedan, *J. Solid State Chem.* **30**, 35 (1979).
17. A. Ahtee, M. Ahtee, A. M. Glazer, and A. W. Hewat, *Acta Crystallogr. B* **32**, 3243 (1976).
18. R. A. Wheeler, M. H. Whangbo, T. Hughbanks, R. Hoffmann, J. K. Burdett, and T. A. Albright, *J. Am. Chem. Soc.* **108**, 2222 (1986).
19. A. M. Glazer, *Acta Crystallogr. A* **31**, 756 (1975).
20. Goldsmith V. M., *Geochemische Verteilungsgesetze der Elemente VII, VIII*, (1927/1928).